

Sulfiphilic Nickel Phosphosulfide Enabled Li₂S Impregnation in 3D Graphene Cages for Li–S Batteries

Guangmin Zhou, Jie Sun, Yang Jin, Wei Chen, Chenxi Zu, Rufan Zhang, Yongcai Qiu, Jie Zhao, Denys Zhuo, Yayuan Liu, Xinyong Tao, Wei Liu, Kai Yan, Hye Ryoung Lee, and Yi Cui*

Lithium-ion batteries (LIBs) have dominated the consumer electronics market for the past two decades. However, the increasing demand of energy storage for portable electronics, large-scale smart grids, and electric vehicles urgently requires the development of reliable batteries with high energy density or specific energy.^[1,2] However, traditional intercalation transition metal-oxide- and phosphate-based cathode materials are approaching their capacity limit and are thus unable to meet these demands. The lithium–sulfur (Li–S) battery, as a next-generation high energy density storage system, has generated great interest due to its high theoretical energy density, high capacity, and the availability of low-cost sulfur.^[3–8] However, Li–S battery technology is still impeded by several issues including low electrical conductivity of sulfur and its discharge products (Li₂S₂/Li₂S), large volume change, and dissolution of lithium polysulfide intermediates during charge/discharge processes. These issues lead to the low utilization of sulfur, poor rate capability, high polarization, as well as reduced Coulombic efficiency and overall energy efficiency.^[9–16]

Encapsulating sulfur into carbon-based materials is an effective strategy to improve the electronic conductivity of the electrode and reduce the dissolution of polysulfide species. Various strategies/materials have been proposed for the effective encapsulation of sulfur, such as hollow carbon nanofiber,^[17] disordered carbon nanotubes,^[18] hollow carbon composites,^[19] double-shelled hollow carbon spheres,^[20] highly ordered meso@microporous carbon structures,^[21] and nitrogen-doped hollow carbon–sulfur structures.^[22] However, as the sublimation temperature of sulfur is low, these strategies must be carried out at low temperature, which inevitably limits the number of suitable synthetic techniques and materials.^[23] For the above designs, an appropriate interior void space or sufficient porosity is necessary to accommodate sulfur's volume expansion during

the lithiation process to prevent destruction of the electrode structure, which further increases the complexity and difficulty of rational electrode structural design. In addition, in order to achieve high energy density, sulfur should be paired with a lithium-metal anode which presents another challenge due to the formation of lithium dendrites caused to the nonuniform deposition of lithium. These dendrites can eventually pierce the separator and lead to short-circuiting within the cell, causing serious safety concerns.^[24–27]

Replacing sulfur with lithium sulfide (Li₂S) is a promising strategy to address the above challenges. The theoretical capacity of Li₂S (1166 mAh g⁻¹) is much higher than that of current commercial cathode materials, and the fully lithiated state (i.e., Li₂S state) avoids the issue of volume expansion during charging.^[28–30] Besides metallic lithium, it can be matched with other nonlithium-containing anode materials such as silicon, germanium, tin, and carbonaceous materials with more reliable safety properties.^[31,32] However, the poor electronic and ionic conductivities of Li₂S, as well as the polysulfide shuttle effect, are still unsolved issues, resulting in poor cycling stability and low capacity.

Many efforts have been made to solve these issues by designing conductive coating layers or improving the contact between Li₂S and electrical conductors; for example, employing high-energy ball milling to mix commercial Li₂S powder with carbon or metal-based materials to improve the conductivity of Li₂S electrode,^[33,34] designing Li₂S–carbon core–shell structures to physically block soluble polysulfides,^[35] and coating metal oxides or sulfides on Li₂S to introduce strong chemical interaction with the Li₂S/lithium polysulfides to prevent shuttle effect.^[36–38] The advantages of the above strategies are mainly summarized in the following: (1) mixing with carbon-based materials improves the electric conductivity; (2) coating by carbon-based layers can physically block soluble polysulfides; (3) coating with polar materials (e.g., metal sulfides^[39,40]) can chemically trap polysulfides. Nevertheless, metal oxides typically exhibit low electrical conductivity and poor mechanical strength, and the high molecular weight of metal oxides leads to a decreased specific capacity. On the other hand, nonpolar carbon cannot efficiently suppress the dissolution and outward diffusion of polar lithium polysulfide species via weak physical adsorption/confinement,^[41,42] resulting in unsatisfactory capacity utilization, rate capability, and long-term cycling stability.

With these considerations in mind, herein, we combine the advantages of both nonpolar carbon materials and polar metal phosphosulfides to stabilize the Li₂S cathode by designing a 3D

Dr. G. Zhou, Dr. J. Sun, Y. Jin, Dr. W. Chen, Dr. C. Zu, Dr. R. Zhang, Dr. Y. Qiu, J. Zhao, D. Zhuo, Y. Liu, Prof. X. Tao, Dr. W. Liu, Dr. K. Yan, Dr. H. R. Lee, Prof. Y. Cui
Department of Materials Science and Engineering
Stanford University
Stanford, CA 94305, USA
E-mail: yicui@stanford.edu
Prof. Y. Cui
Stanford Institute for Materials and Energy Sciences
SLAC National Accelerator Laboratory
2575, Sand Hill Road, Menlo Park, CA 94025, USA



DOI: 10.1002/adma.201603366

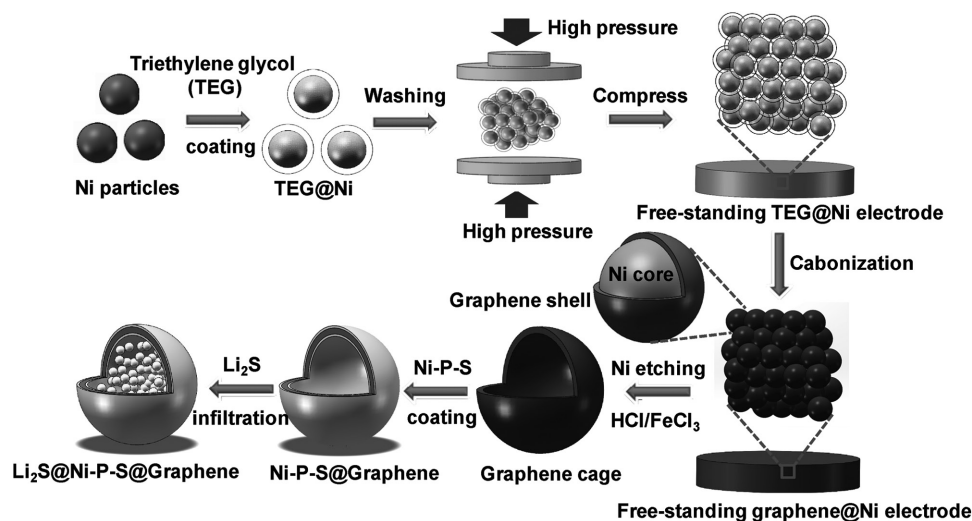


Figure 1. Schematic illustration for the synthesis of Li_2S impregnated 3D Ni-P-S-coated graphene cages.

graphene cage with a thin layer of electrodeposited nickel phosphosulfides (denoted as Ni-P-S) for Li_2S impregnation, which has fivefold advantages: (1) Ni-P-S, as a novel and effective encapsulation material, is highly conductive and can improve the electrical connectivity within the electrode; (2) the polar/hydrophilic nature of Ni-P-S favors the impregnation of Li_2S and allows the formation of strong chemical bond with lithium polysulfides; (3) the electrodeposition method produces an ultrathin coating of Ni-P-S, which has little influence on its specific capacity, and also minimizes the diffusion distance of both lithium ions and electrons, resulting in enhanced rate performance; (4) the small size and uniform distribution of Li_2S reduce the energy barrier; (5) the 3D graphene framework facilitates the transport of electrons and provides a physical barrier to confine Li_2S /lithium polysulfides. By constructing a unique dual-encapsulation nanostructure, significantly improved capacity, long-term cycling stability, and rate capability along with a lowered voltage barrier were achieved.

Figure 1 shows the schematic illustration for the fabrication of Li_2S impregnated 3D Ni-P-S-coated graphene (Ni-P-S@G) cage electrodes. The synthesis details are described in the “Experimental Section.” Commercial Ni particles were used as both template and catalyst to synthesize the conductive network of graphene cages. First, triethylene glycol (TEG) was used to coat the surface of the Ni particles (TEG@Ni). After pressing these TEG@Ni particles under high pressure, a binder-free TEG@Ni electrode was obtained; the compaction process can increase the volumetric energy density of the electrode.^[43] Carbonization was then carried out to convert the TEG coating into a graphene shell. The nickel core was etched away by FeCl_3/HCl aqueous solution leaving the graphene cage. Then, an electrochemical deposition method was used to deposit a small amount of Ni-P-S on the surface of the graphene cages (Ni-P-S@G). Finally, commercial Li_2S particles are dissolved in anhydrous ethanol followed by drop casting of the solution into the as-prepared graphene cage. After evaporation of the ethanol solvent, the Li_2S particles were precipitated into the Ni-P-S@G frameworks ($\text{Li}_2\text{S}@Ni-P-S@G$).

Figure 2a shows photographs of the obtained free-standing graphene-based cage electrodes before (top) and after nickel etching (bottom). The graphene-coated Ni electrodes are gray in color with a diameter of 14 mm. After nickel etching, the morphology is retained and the structure remains intact while the color changes from gray to black. Due to the hydrophobic nature of graphene, surface modification was conducted by coating a thin Ni-P-S layer onto the graphene cage via an electrodeposition strategy. To confirm the improved affinity, the water wetting property of the graphene before and after coating was shown in **Figure 2b,c**. A 10 μL water droplet was dropped onto the graphene and Ni-P-S@G membranes. The graphene membrane exhibits a large contact angle of 41° at the water/graphene interface and this angle decreases slightly after 30 s, indicating its poor surface wettability. However, the water wetting behavior was significantly changed after Ni-P-S coating. As shown in **Figure 2c**, the water droplet quickly spreads out on the surface and absorbs suddenly (within 2s) when it contacts the modified graphene membrane, demonstrating its high hydrophilicity which is beneficial for infiltration of the polar Li_2S /ethanol solution. To evaluate the role of Ni-P-S in adsorbing lithium polysulfides, the graphene and Ni-P-S powders (synthesis details are provided in the “Experimental Section”) with the same total surface area were immersed in a 1,3-dioxolane (DOL)/1,2-dimethoxyethane (DME) (1:1, v:v) solution containing 0.005 M Li_2S_6 (overall stoichiometric ratio) as adsorbents for 8 h. As shown in **Figure 2d**, the Ni-P-S exhibits strong polysulfide adsorption capability and the color of the Li_2S_6 solution changes from yellow to nearly transparent. In contrast, graphene demonstrated quite weak polysulfide adsorption effect as the color of the Li_2S_6 solution remains unchanged. The sharp difference in color change indicates that the polar Ni-P-S shows greatly improved affinity to polysulfides with much better adsorption compared to the nonpolar graphene. To quantitatively measure the amount of Li_2S_6 which is adsorbed, 20 μL of the polysulfide solution after exposure to the graphene and Ni-P-S was tested by inductively coupled plasma-optical emission spectroscopy (ICP-OES). It was found that the

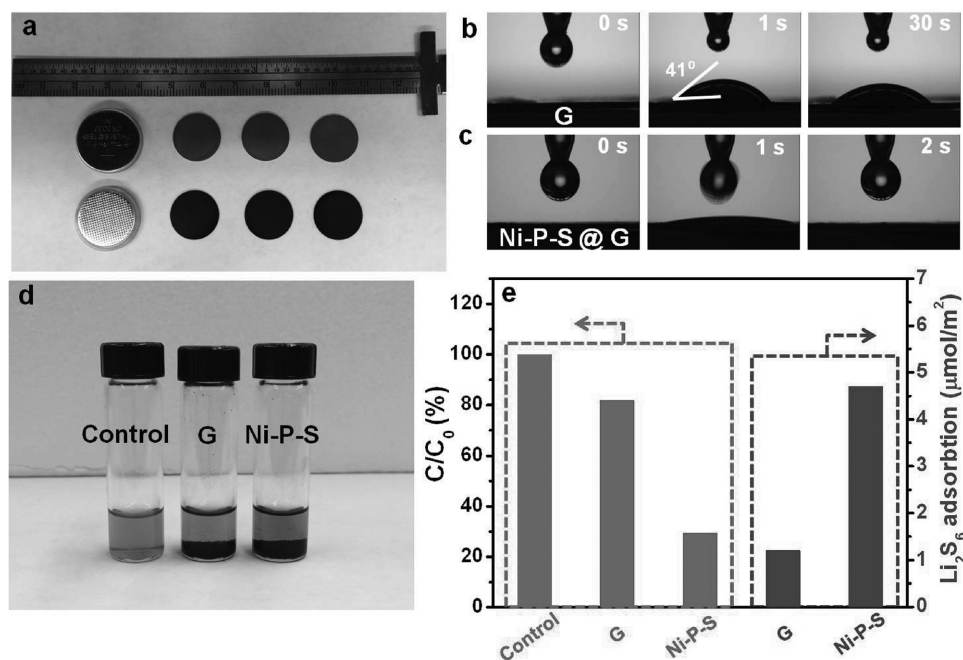


Figure 2. a) Photograph of the free-standing graphene@Ni electrode (top) and graphene electrode (bottom). Surface wetting of the water droplet on the b) graphene and c) Ni–P–S-coated graphene. For Ni–P–S-coated graphene, the water quickly infused into the matrix with good wettability. d) Digital image of the Li_2S_6 (0.005 M) adsorption by the graphene and Ni–P–S in DOL/DME solution. e) Concentration ratio before and after Li_2S_6 adsorption (red bars) and adsorption quantity of Li_2S_6 (blue bars) on the graphene and Ni–P–S.

Li_2S_6 adsorption capacity of Ni–P–S is $4.7 \mu\text{mol m}^{-2}$, approximately four times higher than that of graphene ($1.2 \mu\text{mol m}^{-2}$; Figure 2e). The corresponding sulfur species concentration also confirms that the Ni–P–S coating can remarkably improve the adsorption of lithium polysulfides (Figure 2e), facilitating charge transfer and the electrochemical redox reaction at the adsorption interface.

Scanning electron microscopy (SEM) and transmission electron microscopy (TEM) images (Figures S1a,b and S2a, Supporting Information) show the as-prepared graphene cages with particle size ranging from 1 to 3 μm . These cages adhere to each other forming stacked pores and conductive pathways, which are beneficial for the penetration of electrolyte and fast electron/ion transport. The graphene cage maintains wavy surface features inherited from the shape of the Ni particle template (Figure S3, Supporting Information). The wall thickness of the graphene cage was measured to be 10–20 nm, as shown in Figure S1c (Supporting Information). Benefiting from the compaction and connected network formed by the graphene cages, the electrode retains its free-standing feature. The cross-sectional SEM image of the graphene electrode (Figure S2b, Supporting Information) demonstrates a thickness of around 200 μm with a densely packed porous structure that facilitates electrolyte infiltration. In order to deposit the Ni–P–S (Ni–P or Ni–S) layer, the 3D graphene electrode was dipped in nickel nitrate, sodium hypophosphite, and thiourea (or one of the latter two compounds) mixed solutions. After electrodeposition for a charge of 200 mC (Figure S4, Supporting Information), the Ni–P–S@G exhibits a morphology identical to that before Ni–P–S incorporation (Figures S1d and S2c,d, Supporting Information), while the contrast indicates a thin coating layer

of about 3–5 nm (Figures S1e,f and S5, Supporting Information). X-ray photoelectron spectroscopy (XPS) analysis also clearly shows the successful coating of Ni–P, Ni–S, and Ni–P–S on the surface of graphene from the survey spectrum and Ni 2p, P 2p, S 2p XPS spectra (Figure S6, Supporting Information). The X-ray diffraction (XRD) patterns of the graphene-based cages before and after coating exhibit similar peaks as shown in Figure S7a (Supporting Information), as the ultrathin coating layer is difficult to detect. Energy-dispersive X-ray spectroscopy (EDS) elemental mapping of the Ni–P–S@G cage (Figure S1g–l, Supporting Information) confirms the existence and uniform distribution of Ni, P, and S on the surface of the graphene cage, which is beneficial for improving the affinity of the nonpolar graphene to polar Li_2S /lithium polysulfides.

After surface modification, it is much easier to absorb Li_2S solution within the graphene cages compared with the unmodified graphene cages. Figure 3a shows the SEM image of the graphene cages after Li_2S infiltration (denoted as $\text{Li}_2\text{S}@G$), although some Li_2S can permeate into the void of the cage by capillary force. A large number of Li_2S particles are randomly distributed on the surface of the graphene cage due to the poor hydrophilicity of the graphene surface. In contrast, Figure 3b–d shows the SEM images of the Ni–P-, Ni–S-, and Ni–P–S-coated graphene cages after Li_2S infiltration (denoted as $\text{Li}_2\text{S}@Ni\text{-P}@G$, $\text{Li}_2\text{S}@Ni\text{-S}@G$, and $\text{Li}_2\text{S}@Ni\text{-P-S}@G$). All the surfaces are uniform and smooth, and no visible Li_2S agglomerates are observed, indicating that Li_2S is homogeneously infiltrated and dispersed in these coated graphene cages. The TEM image reveals that the small Li_2S particles were uniformly dispersed inside the graphene cage (Figure 3e). The broadened XRD peaks appearing at 27° , 31° , 45° , and 53° for

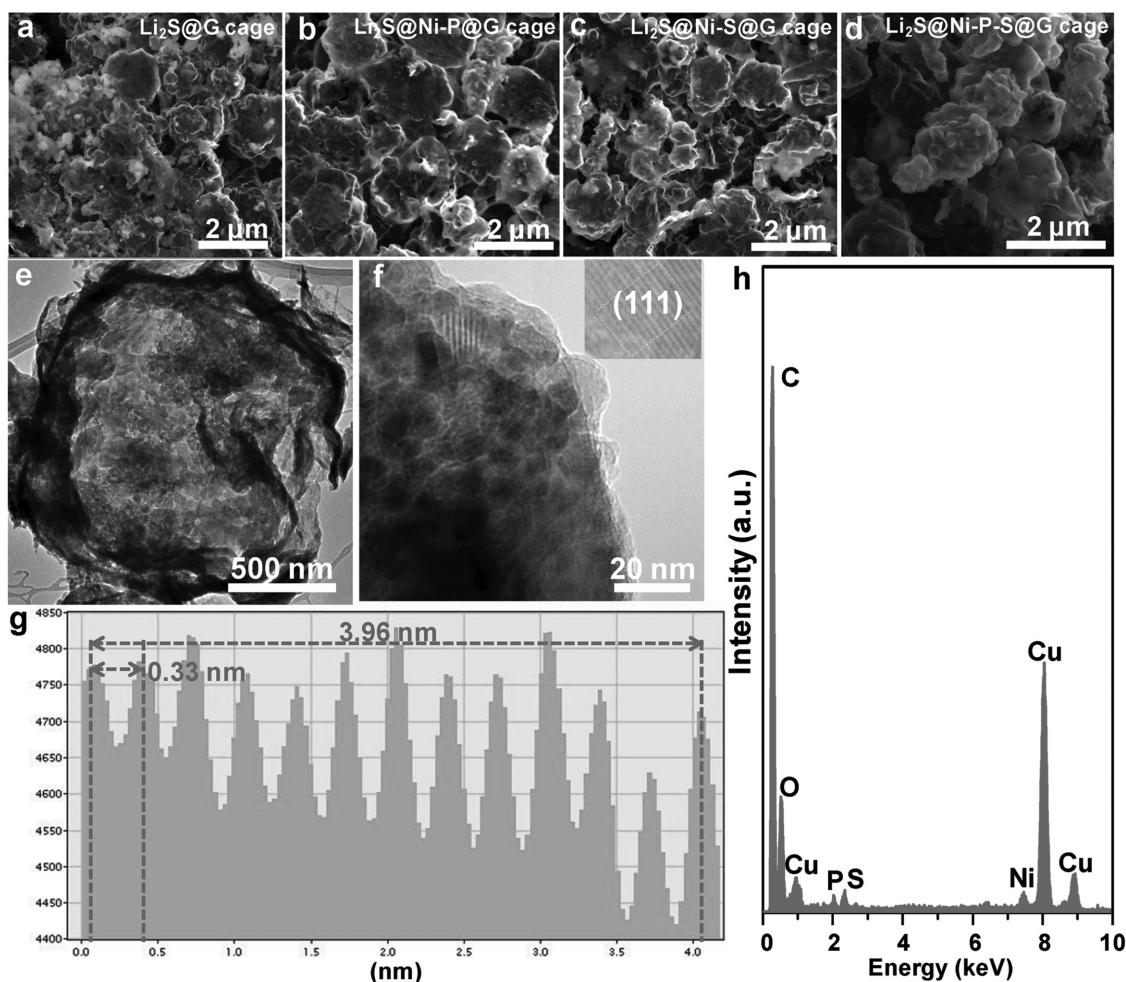


Figure 3. SEM images of the a) $\text{Li}_2\text{S}@G$ cage, b) $\text{Li}_2\text{S}@Ni-P@G$ cage, c) $\text{Li}_2\text{S}@Ni-S@G$ cage, and d) $\text{Li}_2\text{S}@Ni-P-S@G$ cage. e) TEM and f) HRTEM images of the $\text{Li}_2\text{S}@Ni-P-S@G$ cage (inset shows the lattice fringes of Li_2S). g) The intensity plot shows that 12 layers span a distance of 3.96 nm (average interlayer distance: 0.33 nm), corresponding to the (111) plane of Li_2S . h) EDS of the $\text{Li}_2\text{S}@Ni-P-S@G$ cage.

the Li_2S impregnated graphene-based cages compared to commercial Li_2S (Figure S7b, Supporting Information) suggest that the reduced size of the Li_2S particles is beneficial for decreasing the energy barrier of the Li_2S system.^[44,45] The high-resolution TEM (HRTEM) image with a selected area of Li_2S shows lattice fringes with an interplanar spacing of 0.33 nm that exactly corresponds to the (111) plane of Li_2S (Figure 3f,g). EDS clearly confirms the presence of carbon, oxygen, nickel, phosphorous, sulfur, and copper (from the Cu grid) in the $\text{Li}_2\text{S}@Ni-P-S@G$ cage (Figure 3h), indicating the uniform surface coating and successful impregnation of Li_2S into the cage.

To verify the cooperative functions of graphene and Ni-P-S encapsulation on Li_2S cathode, coin cells were assembled to test the electrochemical performance. Contrasting results are obtained regarding positions of the cathodic/anodic peaks in the cyclic voltammetry (CV) profiles, as shown in Figure 4a–d and Figure S8 (Supporting Information). As for the commercial Li_2S , it is not electrochemically active until charged above 3.26 and 3.61 V (anodic peaks: A1 and A2) at 0.1 mV s^{-1} to form lithium polysulfides and sulfur, respectively (Figure 4a), which suggests a sluggish electrochemical redox reaction. However,

some of the Li_2S becomes active after dissolution in ethanol, precipitation, and then encapsulation by the graphene cage. Two anodic peaks reduced by ≈ 0.6 and 0.4 V (compared to commercial Li_2S) located at 2.65 and 3.22 V (Figure 4b) indicate that the kinetics of the reaction has been improved. The peaks are further downshifted to 2.51 (2.53, 2.53) and 2.83 (3.00, 3.15) V for the Li_2S that is treated with ethanol and then encapsulated by the Ni-P-S@G (Ni-P@G, Ni-S@G) cages, respectively (Figure 4c; Figure S8, Supporting Information). This indicates that the better distribution of Li_2S with small size results in a reduced energy barrier for its conversion. The cathodic peaks in the following discharge are comparable for all the cases. For example, the sharp cathodic peaks of the $\text{Li}_2\text{S}@Ni-P-S@G$ electrode at 2.31 V (transition between S and soluble lithium polysulfides (Li_2S_x , $4 \leq x \leq 8$)) and 1.97 V (transition between lithium polysulfides (Li_2S_x , $4 \leq x \leq 8$) and $\text{Li}_2\text{S}/\text{Li}_2\text{S}_2$)^[1,46] indicate favorable kinetics compared with the commercial Li_2S and $\text{Li}_2\text{S}@G$ electrodes. To further compare the reaction kinetics of different electrodes, Figure 4e shows the initially charged curves from open-circuit voltage to 4.0 V. The $\text{Li}_2\text{S}@Ni-P-S@G$ electrode exhibits the lowest and longest voltage plateau at about

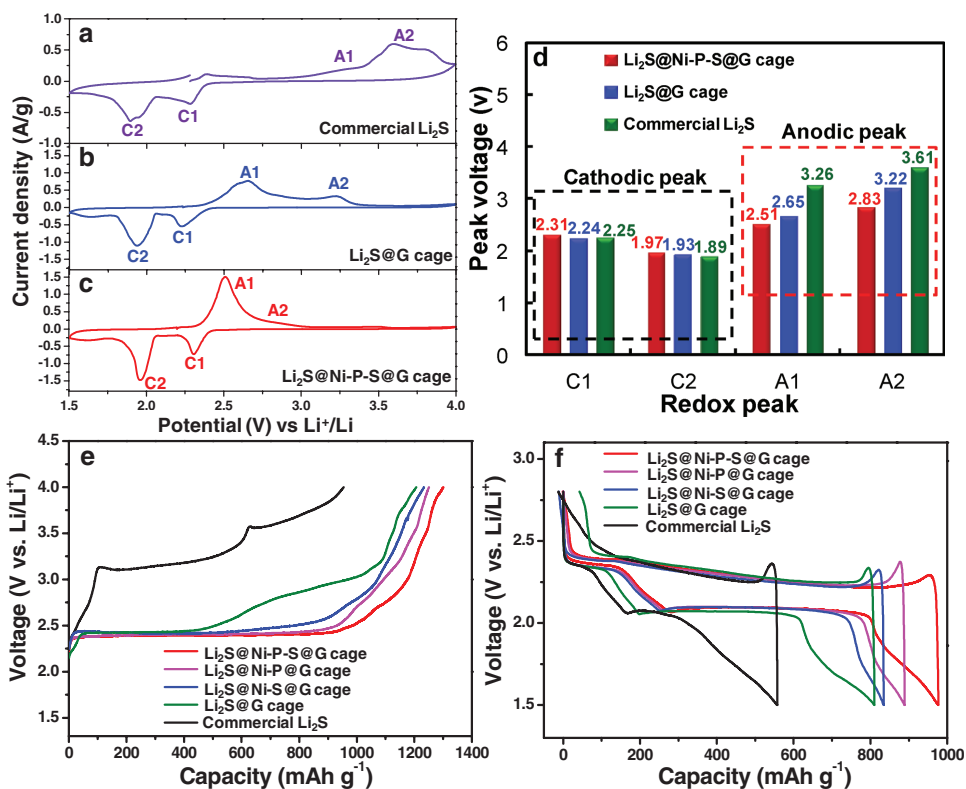


Figure 4. CV profiles of the a) commercial Li₂S, b) Li₂S@G electrode, c) Li₂S@Ni–P–S@G electrode, and d) the corresponding peak voltages of these graphene-based electrodes. e) First charge curves of the commercial Li₂S, Li₂S@G, Li₂S@Ni–S@G, Li₂S@Ni–P@G, and Li₂S@Ni–P–S@G electrodes from open-circuit voltage to 4 V. f) Charge/discharge curves of the commercial Li₂S, Li₂S@G, Li₂S@Ni–S@G, Li₂S@Ni–P@G, and Li₂S@Ni–P–S@G electrodes at 0.1 C rate.

2.4 V with almost invisible potential barrier during the first charge as it has the lowest charge-transfer resistance among all electrodes, in good agreement with the electrochemical impedance spectroscopy (EIS) results (Figure S9, Supporting Information). A similar charging phenomenon is observed for Li₂S@G, Li₂S@Ni–S@G, and Li₂S@Ni–P@G electrodes. For the commercial Li₂S electrode, two apparent potential barriers appeared during the charging process, indicating a sluggish activation process, which matches well with the CV results. Figure 4f shows the second galvanostatic charge–discharge profiles of these electrodes within the potential window of 1.5–2.8 V at 0.1 C rate. The Li₂S@Ni–P–S@G electrode demonstrates the highest discharge capacity and smallest voltage hysteresis compared to the other electrodes, indicating much improved Li₂S utilization and redox kinetics. The high electrical conductivity of the graphene and Ni–P–S facilitates the polysulfide redox kinetics as well as the small size of Li₂S, contributing to the dramatically improved performance.

Figure 5a and Figure S10 (Supporting Information) show the discharge/charge profiles of these cathodes under various C rates from 0.1 up to 4 C. The polarization in the Li₂S@Ni–P–S@G cathode is much alleviated compared to the other cathodes and this phenomenon becomes more distinct with increased current density (Figure 5c). The reversible discharge capacity of Li₂S@Ni–P–S@G cathode is around 980 mAh g^{−1} at 0.1 C (based on the Li₂S mass), and the overall capacity of the Li₂S@Ni–P–S@G cathode is 594 mAh g^{−1} as calculated

according to the Li₂S mass ratio (60.6 wt%, including the weight of Ni–P–S and graphene cages; see the “Experimental Section”). The capacity gradually decreases to 728, 665, 624, and 543 mAh g^{−1} (441, 403, 378, and 329 mAh g^{−1} based on the whole electrode) as the current rate increases to 0.5, 1, 2, and 4 C, respectively (Figure 5a,b; Figure S10, Supporting Information), demonstrating excellent rate performance. The rate capability is much better than that of the Li₂S@G, Li₂S@Ni–S@G, Li₂S@Ni–P@G electrodes (Figure S11, Supporting Information), and overwhelmingly better than that of commercial Li₂S cathode with values of only 556, 183, 117, 78, and 43 mAh g^{−1} (overall capacities of commercial Li₂S cathode are 389, 128, 82, 55, and 30 mAh g^{−1} including the weight of polyvinylidene difluoride (PVDF) and carbon black) tested under the same conditions. When the current rate is abruptly changed back to 0.5 C rate again, the Li₂S@Ni–P–S@G electrode is able to recover to the original capacity, demonstrating excellent structural stability of the dual encapsulated electrode design. The cycling performance was measured at 0.3 C rate between 1.5 and 2.8 V for 100 cycles, as shown in Figure 5d. The Li₂S@Ni–P–S@G electrode exhibits good cycling stability with nearly 100% Coulombic efficiency and a reversible specific capacity of 670 mAh g^{−1} after 100 cycles, much higher than that of the commercial Li₂S, Li₂S@G, Li₂S@Ni–S@G, and Li₂S@Ni–P@G electrodes with capacities of 88, 376, 505, and 540 mAh g^{−1}, respectively. The fast capacity decay of the commercial Li₂S and Li₂S@G electrodes should be ascribed to

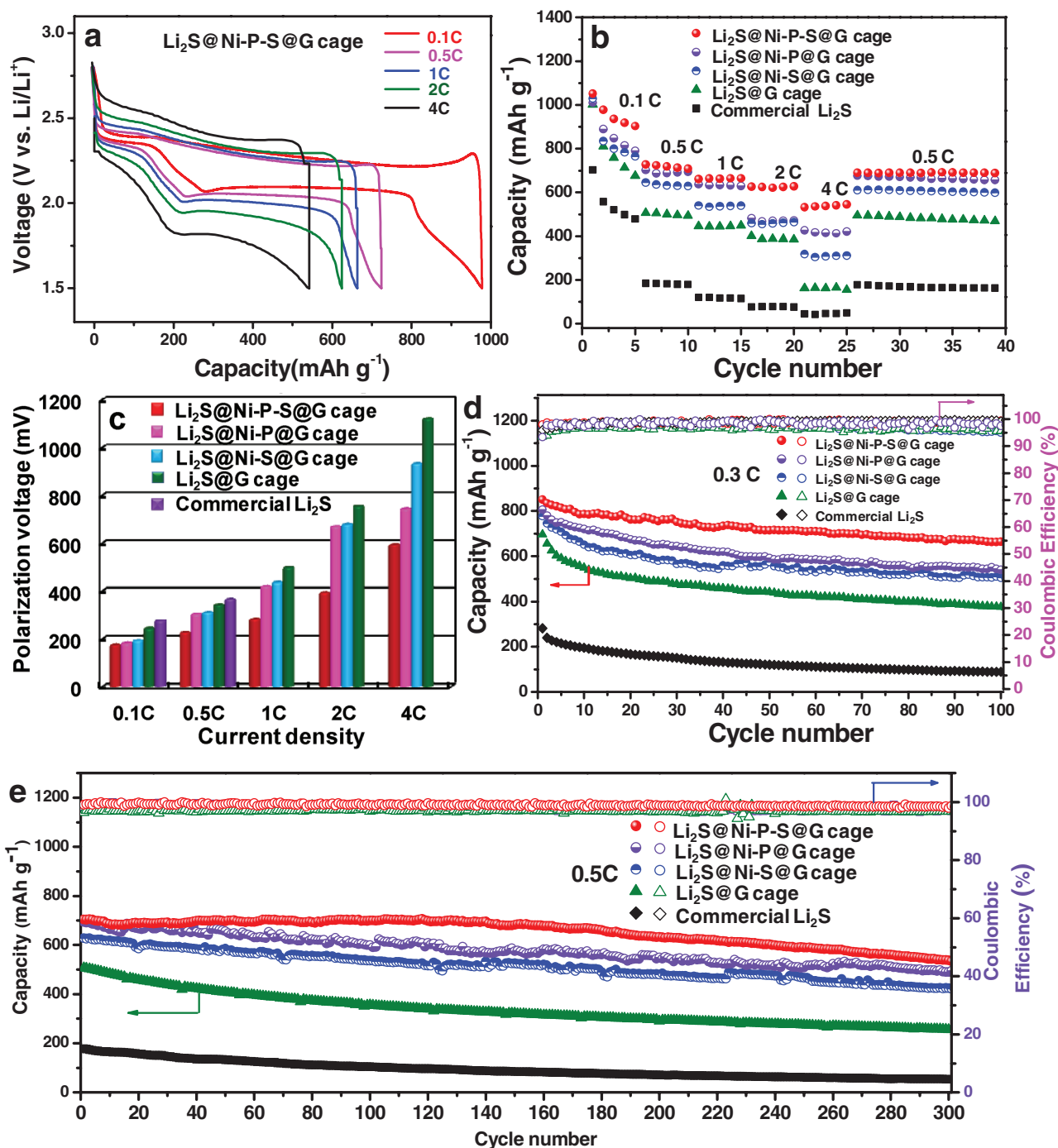


Figure 5. a) Charge/discharge voltage profiles of the $\text{Li}_2\text{S}@Ni-P-S@G$ electrode at various rates. b) Rate performance of the commercial Li_2S , $\text{Li}_2\text{S}@G$, $\text{Li}_2\text{S}@Ni-S@G$, $\text{Li}_2\text{S}@Ni-P@G$, and $\text{Li}_2\text{S}@Ni-P-S@G$ electrodes at different current densities. c) Comparison of the polarization voltage between the charge and discharge plateaus at different current densities. d) Cycling performance and Coulombic efficiency of the commercial Li_2S , $\text{Li}_2\text{S}@G$, $\text{Li}_2\text{S}@Ni-S@G$, $\text{Li}_2\text{S}@Ni-P@G$, and $\text{Li}_2\text{S}@Ni-P-S@G$ electrodes at 0.3 C for 100 cycles. e) Long-term cycle stability of the corresponding electrodes at 0.5 C for 300 cycles after the rate capability test.

the rapid dissolution of lithium polysulfides into the electrolyte. To elucidate whether Li ion will react with Ni-P-S during the discharge process, the electrochemical reactivity of Ni-P-S was tested between 1.5 and 2.8 V. It is noted that the first discharge capacity of Ni-P-S is 68 mAh g^{-1} , and the capacity remains only 5.8 mAh g^{-1} after 100 cycles (Figure S12, Supporting

Information). In addition, the Ni-P-S only accounts for 9.1 wt% of the whole electrode. Together, these points demonstrate that Ni-P-S contributes very little to the overall capacity. To further evaluate the long-term cycle life of these electrodes, the cells were tested at 0.5 C for over 300 cycles after the rate capability test (Figure 5e). The $\text{Li}_2\text{S}@Ni-P-S@G$, $\text{Li}_2\text{S}@$

Ni-P@G, and Li₂S@Ni-S@G electrodes demonstrate fairly stable cycling performance with stable Coulombic efficiency approaching 100% and retain discharge capacities of 540, 490, and 425 mAh g⁻¹ after 300 cycles. In sharp contrast, the commercial Li₂S and Li₂S@G electrodes exhibit poor cycling performance with capacities of only 53 and 256 mAh g⁻¹, respectively. The capacity retention of the Li₂S@Ni-P-S@G (77.3%) with an average capacity decay of only 0.076% per cycle was superior to those of the Li₂S@Ni-P@G, Li₂S@Ni-S@G, Li₂S@G, and commercial Li₂S electrodes with capacity retentions of 70.6%, 67.8%, 50.6%, and 29.4%, which correspond to capacity decay of 0.098%, 0.107%, 0.165%, and 0.235% per cycle, respectively. The highly improved cycling and rate performance reveal that the Ni-P-S-coated graphene cage network facilitates electron/ion transport pathways and improves the reaction kinetics. The hydrophilic Ni-P-S/Ni-P/Ni-S binds favorably with polysulfide anions and can effectively suppress the dissolution and leakage of lithium polysulfides after extensive cycling, thereby improving the long-term cycling stability.

Considering the unique structure of the free-standing graphene cage, we propose a dual-layer design to further increase the active material loading of the electrode to 5.2 mg cm⁻² by stacking one layer of Li₂S@Ni-P-S@G electrode on top of another. The discharge curves of the dual-layer Li₂S@Ni-P-S@G electrode demonstrate two well-retained plateaus from 0.1 C to even a high rate of 2 C, as shown in Figure S13a (Supporting Information), indicating the excellent reaction kinetics. This design enables the battery to deliver a high capacity of 943 mAh g⁻¹ at 0.1 C rate, corresponding to a high areal capacity of 4.9 mAh cm⁻² for the Li₂S cathode, which is close to the areal capacity of high-energy commercially available LIB cathodes (such as LiCoO₂, ≈3–5 mAh cm⁻²).^[47] Although the voltage of Li-S batteries is half that of the commercial LIBs, which compromises the overall areal energy density, there is a great potential to further improve the energy density of Li-S batteries to 2–3 times higher specific energy of LIBs by rational designing electrode structure, tuning the electrolyte and sulfur ratio, optimizing electrolytes and separators, and protecting metallic lithium anode. Moreover, they exhibit good rate performance with reversible discharge capacities reaching 546 and 340 mAh g⁻¹ at large current densities of 1 and 2 C (Figure S13b, Supporting Information). In addition, the dual-layer cathode delivers an initial discharge capacity of 703 mAh g⁻¹ at 0.5 C rate, which stabilizes at around 430 mAh g⁻¹ after 300 cycles, corresponding to a capacity decay of ≈0.13% per cycle (Figure S13c, Supporting Information), which is also comparable to or better than the performance of most of the reported Li₂S cathodes with a lower mass loading, demonstrating its superior cycling stability.

To substantiate the effective Li₂S/lithium polysulfide trapping by this unique structural design, Li₂S@G and Li₂S@Ni-P-S@G cathodes were disassembled in a charged state after 100 cycles, washed with DME, and investigated by SEM. The surface of the Li₂S@G electrode became quite rough and covered with many sulfur species (Figure S14a,b, Supporting Information), indicating the dissolution and diffusion of the polysulfides into the electrolyte due to weak binding between graphene and lithium polysulfides during cycling. In contrast, the morphology and microstructure of the Li₂S@Ni-P-S@G

electrode is well retained, the sulfur species are encapsulated in the graphene cage and strongly adsorbed by the Ni-P-S coating layer (Figure S14c,d), demonstrating the effectiveness of the structural design which confines sulfur species through a combined physical and chemical method for stabilized sulfur chemistry. Additional evidence of the effective prevention of lithium polysulfide dissolution is revealed by the postmortem analysis of the Li anode. After cycling paired with an Li₂S@G cathode, the lithium-metal anode exhibited serious deterioration with a rough surface and a large number of Li dendrites, as shown in Figure S15a,b (Supporting Information). The degraded lithium-metal surface is a result of the parasitic reactions between the metallic lithium and dissolved lithium polysulfide during cycling. By contrast, a relatively smooth and intact lithium-metal surface is observed from the top surface when employing an Li₂S@Ni-P-S@G cathode (Figure S15c,d, Supporting Information), suggesting that the cathode structure effectively absorbs polysulfide and prevents dissolved polysulfides from diffusing out into the electrolyte and reacting with the lithium metal, thereby alleviating lithium-surface damage and reducing the accumulation and aggregation of the discharge products Li₂S/Li₂S₂ on the lithium-metal anode.

In order to gain deeper insights into the improved cycle performance and rate capability, density functional theory (DFT) calculations were performed to examine the interaction between Li₂S and these nickel-based compounds. NiS, Ni₂P, and Ni(PS₃)₂ were chosen as the typical stable examples from nickel sulfides, nickel phosphides, and nickel phosphosulfides, respectively. The binding energies (*E*_b) of Li₂S with graphene, NiS, Ni₂P, and Ni(PS₃)₂, respectively, were obtained by a CASTEP simulation package in the framework of DFT. We consider the entrapment of Li₂S and calculate the binding energy of both the chemical bond and the physical van der Waals (vdW) interaction, as summarized in Figure 6 and Table S1 (Supporting Information). It is important to include the physical interaction of these materials, especially for weak anchoring material as its contribution to the total binding energy can be more than 25%.^[48] The vdW interaction also significantly affects the configuration of the sequestered lithium polysulfide species and plays an important role at the beginning of the lithiation stage. It is apparent from the calculation that all three compounds have sizeable binding energies (*E*_b) for Li₂S. According to the values of *E*_b, Ni(PS₃)₂ exhibits the largest binding strength (3.36 eV), which is about twice that of the other two species (NiS, 1.26 eV; Ni₂P, 1.43 eV) because both of the exposed S and P atoms in the layer of Ni(PS₃)₂ strongly interact with Li and S atoms, respectively, whereas only the S atom interacts with the lithium atom in the case of NiS. Even though both the Ni and P atoms from Ni₂P interact with the Li₂S molecule, the binding energy is lower than Ni(PS₃)₂. In addition, all the binding energies are much higher than that for graphene layer (0.61 eV) and solvent (DOL/DME, 0.85 eV).^[49] According to the definition, a higher binding energy indicates a more energetically favorable reaction, leading to trapping of soluble polysulfides with improved battery performance.

In summary, we have developed a unique 3D interconnected graphene cage structure with a thin sulfiphilic Ni-P-S coating layer allowing for Li₂S impregnation. The close compacted graphene cages form an excellent conducting network inside the

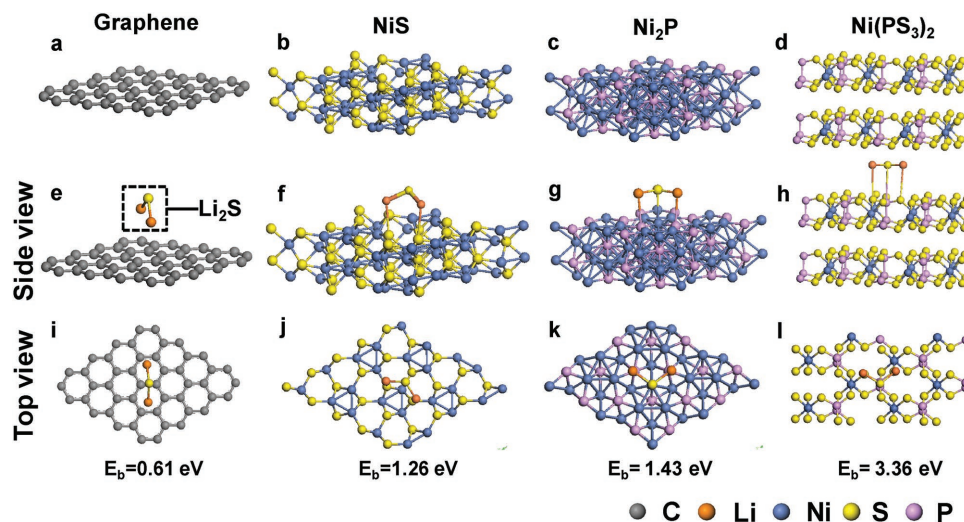


Figure 6. Side views of a) graphene, b) NiS, c) Ni₂P, and d) Ni(PS₃)₂. Side views of e) graphene, f) NiS, g) Ni₂P, and h) Ni(PS₃)₂ binding with Li₂S. Top views of i) graphene, j) NiS, k) Ni₂P, and l) Ni(PS₃)₂ binding with Li₂S. Gray, orange, blue, yellow, and purple balls represent, respectively, C, Li, Ni, S, and P atoms. The calculated binding energies with van der Waals interaction for Li₂S with graphene, NiS, Ni₂P, and Ni(PS₃)₂, respectively, were shown below accordingly.

electrode, avoiding the use of any conductive additives and binders, and promoting highly efficient utilization of the Li₂S cathode. The small size and uniform distribution of Li₂S significantly reduce the Li-ion diffusion barrier, and the strong hydrophilicity/polarity of Ni–P–S and lithium (poly)sulfides effectively suppresses the outward immigration of polysulfide species. Through the unique dual-encapsulation nanostructure design, we have further increased the active material loading of the electrode to 5.2 mg cm⁻². The feasible combination of a graphene framework as a physical barrier and a sulfiphilic coating as a chemical bonding layer yields a high specific capacity of 980 mAh g⁻¹ at 0.1 C rate, a high-rate capacity of 543 mAh g⁻¹ at 4 C rate, and excellent cycling stability over 300 cycles with an extremely low capacity decay rate of ≈0.076% per cycle. This approach will shed light on the rational design of Li₂S-based materials with unique encapsulation materials and architectures, providing invaluable guidance for the development of high-performance Li–S batteries for practical applications.

Experimental Section

Synthesis of 3D Free-Standing Graphene Cage: Ni particles were used as both the catalyst to grow graphene and the template to form the graphene cage with internal void. In detail, 3 g of Ni particles (Alfa Aesar) was dispersed in 40 mL hydrochloric acid (1 M) for 5 min to remove the oxide layer on the surface, washed with water/ethanol, and then dried in the oven for 0.5 h. The obtained Ni particles were then dispersed in 200 mL of TEG (Sigma Aldrich) mixed with 0.5 mL of 50% w/w aqueous NaOH solution to facilitate the decomposition of TEG and formation of a uniform carbon atom adsorption layer on the surface.^[50] After stirring at 215 °C for 8 h, the conformally coated Ni particles were collected by centrifugation, and washed several times with ethanol and acetone alternately. After drying in a vacuum oven at 60 °C for 1 h, the as-obtained conformally coated Ni particles were pressed into free-standing pellets with a dry press machine (MTI, Inc.) at 20 MPa. The compressed pellets were placed in a tube furnace, heated to 450 °C at 10 °C min⁻¹ under Ar atmosphere and annealed at 450 °C to catalyze

graphene growth for 1 h and to strongly bridge the graphene-coated Ni particles together. An Ar flow rate of 80 sccm was maintained during the annealing process. The Ni catalysts were etched away by immersing the free-standing pellets into a FeCl₃ aqueous solution (1 M FeCl₃ with 0.5 M HCl). Then the 3D free-standing graphene cages were obtained after washing with 0.1 M HCl and ethanol, and drying on a hot plate at 60 °C for 2 h.

Synthesis of Ni–P–S-, Ni–P-, and Ni–S-Coated Graphene Cages: The Ni–P–S-, Ni–P-, and Ni–S-coated graphene cages were produced by an electrochemical deposition method using a three-electrode system with free-standing graphene cages as working electrode, a saturated calomel electrode as reference electrode, and a platinum net as counter electrode in a water/ethanol solution containing corresponding nickel, phosphorus, and sulfur sources. The graphene electrode was first wetted by ethanol before electrodeposition. The solutions used were 50 × 10⁻³ M nickel nitrate (Ni(NO₃)₂·6H₂O), 500 × 10⁻³ M sodium hypophosphite (NaH₂PO₂·H₂O), and 500 × 10⁻³ M thiourea (CH₄N₂S) for depositing Ni–P–S; 50 × 10⁻³ M nickel nitrate and 500 × 10⁻³ M sodium hypophosphite for depositing Ni–P; and 50 × 10⁻³ M nickel nitrate and 500 × 10⁻³ M thiourea for depositing Ni–S. The electrodeposition process was conducted by applying –1.1 V with respect to the reference electrode for a coulomb of 200 mC. After electrodeposition, the coated graphene electrode was rinsed with water and ethanol several times to remove the residual solution and then dried in the oven at 60 °C for 3 h.

Synthesis of Ni–P–S: The Ni–P–S was prepared using the same procedures as outlined above except a thin stainless steel foil was used as working electrode instead of graphene cages. The electrodeposition process was conducted by applying –1.1 V with respect to the reference electrode for 10 h. After electrodeposition, the Ni–P–S-coated stainless steel foil was sonicated to peel off the Ni–P–S powder. The obtained Ni–P–S powder was washed with water and ethanol several times and then dried in the oven at 60 °C for 3 h.

Synthesis of Li₂S Impregnated 3D Graphene-Based Cages: Commercial Li₂S powder (99.5%, Alfa Aesar) was dissolved in anhydrous ethanol and stirred overnight at room temperature inside an argon-sealed glove box to obtain a 0.55 M Li₂S solution. The free-standing graphene-based cages were first dried at 100 °C in the glove box (O₂ and H₂O concentration < 0.1 ppm) overnight before impregnating the Li₂S solution. To infiltrate the Li₂S solution, the graphene cage and Ni–P–S-, Ni–P-, and Ni–S-coated graphene cages were placed within a stainless steel cell cap and heated to 260 °C over a hot plate. Li₂S solution (25 μL)

was slowly added into the graphene cages until the ethanol had visibly evaporated to ensure rapid nucleation of Li_2S with a small size. The process was repeated, switching between each face with 50 μL of 0.55 M Li_2S solution used in total. These samples were heated at 260 °C for 30 min to completely evaporate off the ethanol and precipitate an even Li_2S coating into the graphene cage frameworks.

Materials Characterization: The morphologies of the samples were investigated by an FEI XL30 Sirion SEM operated at an accelerating voltage of 5 kV. Microstructure characterization and scanning TEM elemental mapping were carried out by an FEI Tecnai G2 F20 X-TWIN TEM at 200 kV. Crystal structure characterization was performed with a Panalytical X'Pert diffractometer with Cu $K\alpha$ radiation ($\lambda = 0.154056$ nm) between 10° and 70° at a scan rate of 0.04° s^{-1} . Kapton film was used to protect the air-sensitive Li_2S impregnated graphene-based cages during the characterization. ICP-OES was performed by inductively coupled plasma-mass spectrometry (Thermo Scientific ICAP 6300 Duo View Spectrometer). XPS analysis was performed on an SSI SProbe XPS spectrometer with monochromatic Al $K\alpha$ (1486.6 eV) radiation.

Adsorption Test: The polysulfide catholyte (Li_2S_6) was prepared by chemically reacting sublimed sulfur and an appropriate amount of lithium sulfide in 1,3-dioxolane/1,2-dimethoxyethane solution (1:1 by volume) to form Li_2S_6 (1.0 M) in the solution. The solution was then stirred at 70 °C in an Ar-filled glove box overnight to produce a brownish-red Li_2S_6 catholyte solution. The Li_2S_6 solution was then diluted to 0.005 M for the polysulfide capture test. After the immersion of the samples in 0.005 M Li_2S_6 for 8 h, 20 μL of the solution was transferred for ICP-OES testing.^[51]

Electrochemical Measurements: Electrochemical experiments were performed using CR2032 coin cells assembled in an argon-filled glove box with lithium metal as the counter and reference electrodes. The Ni–P–S electrode was prepared by mixing Ni–P–S active material, carbon black, and PVDF in the ratio of 6:2:2 in *N*-methyl-2-pyrrolidone to form a slurry that was pasted onto carbon-coated aluminum foil. The commercial Li_2S cathode was prepared by mixing 70 wt% of the Li_2S active material, 20 wt% carbon black conductive additives, and 10 wt% PVDF in *N*-methyl-2-pyrrolidone to form a slurry that was pasted onto carbon-coated aluminum foil. The Li_2S electrode was cut into circular discs with a diameter of 12 mm and used as a cathode. The electrolyte was prepared by dissolving an appropriate amount of lithium bis(trifluoromethanesulfonyl)imide (1 M) in 1:1 v/v DME and DOL containing LiNO_3 (0.1 M). About 20 μL of the electrolyte containing a polysulfide ($[\text{S}] = 0.2$ M, ≈ 0.18 mg of Li_2S) was added to wet the Li_2S impregnated graphene-based cathode. The Celgard 2400 separator was then placed over the electrode and an additional 20 μL of the blank electrolyte was added to the cell. The lithium-metal foil anode was placed on top of the separator. The Li_2S impregnated graphene-based cages were used as self-supported cathode materials with an Li_2S loading of ≈ 2 mg cm^{-2} including the mass of the polysulfide additive. The corresponding weight percents of Li_2S , graphene cage, and Ni–P–S are 60.6%, 30.3%, and 9.1%, respectively. For the high Li_2S loading cathode, 50 μL of Li_2S solution (0.55 M) was slowly added into the Ni–P–S@G cages until the ethanol was evaporated, and the dual-layer cathode was prepared by stacking one $\text{Li}_2\text{S}@Ni\text{-P-S}@G$ electrode on the top of the other one, followed by adding 20 μL of the polysulfide ($[\text{S}] = 0.6$ M, ≈ 0.55 mg of Li_2S) containing electrolyte on each layer. The corresponding Li_2S loading was 5.2 mg cm^{-2} in the cathode including the mass of the polysulfide additive. Galvanostatic cycling measurements were evaluated with an Arbin battery cycler. The cells were initially charged from open-circuit voltage to 4.0 V (vs Li/Li^+) and then cycled between 1.5 and 2.8 V at room temperature. The current densities were varied between 0.1 C and 4 C rates, and calculated specific capacities were based on the mass of Li_2S in the cathode unless specially indicated in the text. Cyclic voltammetry measurements were performed on a VMP3 potentiostat (Bio-logic) from open-circuit voltage to 4.0 V in the initial cycle and then from 1.5 to 2.8 V in the following cycles with a scan rate of 0.1 mV s^{-1} . EIS data were obtained with a VMP3 potentiostat (Bio-logic) from 200 KHz to 100 mHz with an AC voltage amplitude of 10 mV at the open-circuit potential.

Simulation Methods: First-principles calculations are performed within the DFT framework, as implemented in CASTEP package. The electron exchange and correlation interaction is described by the generalized gradient approximation method. The following valence electron configurations were used: Ni ($3d^8 4s^2$), P ($3s^2 3p^3$), S ($3s^2 3p^4$), C ($2s^2 2p^2$), and Li ($2s^1$). After checking for convergence, 450 eV was chosen as the cutoff energy of the plane-wave basis for the Kohn–Sham states. All atomic positions and lattice vectors were fully optimized using a conjugate gradient algorithm to obtain the unstrained configuration. Atomic relaxation was performed until the change of total energy was less than 10^{-5} eV and all the forces on each atom were smaller than 0.01 eV \AA^{-1} .

Supporting Information

Supporting Information is available from the Wiley Online Library or from the author.

Acknowledgements

G.Z. and J.S. contributed equally to this work. This work was supported by the Joint Center for Energy Storage Research (JCESR), a battery hub under the US Department of Energy. The authors thank Dr. L. Liao and Mr. Y. Li for helpful discussions.

Received: June 27, 2016
Revised: December 13, 2016
Published online:

- [1] Y. Yang, G. Zheng, Y. Cui, *Chem. Soc. Rev.* **2013**, *42*, 3018.
- [2] P. G. Bruce, S. A. Freunberger, L. J. Hardwick, J.-M. Tarascon, *Nat. Mater.* **2012**, *11*, 19.
- [3] S. Evers, L. F. Nazar, *Acc. Chem. Res.* **2013**, *46*, 1135.
- [4] A. Manthiram, S.-H. Chung, C. Zu, *Adv. Mater.* **2015**, *27*, 1980.
- [5] D.-W. Wang, Q. Zeng, G. M. Zhou, L. Yin, F. Li, H.-M. Cheng, I. R. Gentle, G. Q. M. Lu, *J. Mater. Chem. A* **2013**, *1*, 9382.
- [6] R. Xu, J. Lu, K. Amine, *Adv. Energy Mater.* **2015**, *5*, 1500408.
- [7] Y. X. Yin, S. Xin, Y. G. Guo, L. J. Wan, *Angew. Chem. Int. Ed.* **2013**, *52*, 13186.
- [8] L. Ma, K. E. Hendrickson, S. Wei, L. A. Archer, *Nano Today* **2015**, *10*, 315.
- [9] Z. Seh, W. Li, J. J. Cha, G. Zheng, Y. Yang, M. T. McDowell, P.-C. Hsu, Y. Cui, *Nat. Commun.* **2013**, *4*, 1331.
- [10] J.-Q. Huang, Q. Zhang, F. Wei, *Energy Storage Mater.* **2015**, *1*, 127.
- [11] X. L. Ji, K. T. Lee, L. F. Nazar, *Nat. Mater.* **2009**, *8*, 500.
- [12] R. Elazari, G. Salitra, A. Garsuch, A. Panchenko, D. Aurbach, *Adv. Mater.* **2011**, *23*, 5641.
- [13] H.-J. Peng, T.-Z. Hou, Q. Zhang, J.-Q. Huang, X.-B. Cheng, M.-Q. Guo, Z. Yuan, L.-Y. He, F. Wei, *Adv. Mater. Interfaces* **2014**, *1*, 1400227.
- [14] L. Li, Z. P. Wu, H. Sun, D. Chen, J. Gao, S. Suresh, P. Chow, C. V. Singh, N. Koratkar, *ACS Nano* **2015**, *9*, 11342.
- [15] G. Zhou, E. Paek, G. S. Hwang, A. Manthiram, *Nat. Commun.* **2015**, *6*, 7760.
- [16] L. Qie, A. Manthiram, *Adv. Mater.* **2015**, *27*, 1694.
- [17] G. Y. Zheng, Y. Yang, J. J. Cha, S. S. Hong, Y. Cui, *Nano Lett.* **2011**, *11*, 4462.
- [18] J. C. Guo, Y. H. Xu, C. S. Wang, *Nano Lett.* **2011**, *11*, 4288.
- [19] N. Jayaprakash, J. Shen, S. S. Moganty, A. Corona, L. A. Archer, *Angew. Chem. Int. Ed.* **2011**, *50*, 5904.
- [20] C. Zhang, H. B. Wu, C. Yuan, Z. Guo, X. W. Lou, *Angew. Chem. Int. Ed.* **2012**, *51*, 9592.
- [21] Z. Li, Y. Jiang, L. Yuan, Z. Yi, C. Wu, Y. Liu, P. Strasser, Y. Huang, *ACS Nano* **2014**, *8*, 9295.

- [22] W. Zhou, X. Xiao, M. Cai, L. Yang, *Nano Lett.* **2014**, *14*, 5250.
- [23] F. Wu, J. T. Lee, E. Zhao, B. Zhang, G. Yushin, *ACS Nano* **2016**, *10*, 1333.
- [24] G. Zhou, E. Paek, G. S. Hwang, A. Manthiram, *Adv. Energy Mater.* **2016**, *6*, 1501355.
- [25] Y. Qiu, G. Rong, J. Yang, G. Li, S. Ma, X. Wang, Z. Pan, Y. Hou, M. Liu, F. Ye, W. Li, Z. W. Seh, X. Tao, H. Yao, N. Liu, R. Zhang, G. Zhou, J. Wang, S. Fan, Y. Cui, Y. Zhang, *Adv. Energy Mater.* **2015**, *5*, 1501369.
- [26] R. Cao, W. Xu, D. Lv, J. Xiao, J.-G. Zhang, *Adv. Energy Mater.* **2015**, *5*, 1402273.
- [27] L. Suo, Y. Zhu, F. Han, T. Gao, C. Luo, X. Fan, Y.-S. Hu, C. Wang, *Nano Energy* **2015**, *13*, 467.
- [28] Y. Yang, G. Y. Zheng, S. Misra, J. Nelson, M. F. Toney, Y. Cui, *J. Am. Chem. Soc.* **2012**, *134*, 15387.
- [29] C. Zu, M. Klein, A. Manthiram, *J. Phys. Chem. Lett.* **2014**, *5*, 3986.
- [30] Y. Son, J.-S. Lee, Y. Son, J.-H. Jang, J. Cho, *Adv. Energy Mater.* **2015**, *5*, 1500110.
- [31] Y. Yang, M. T. McDowell, A. Jackson, J. J. Cha, S. S. Hong, Y. Cui, *Nano Lett.* **2010**, *10*, 1486.
- [32] J. Hassoun, B. Scrosati, *Angew. Chem. Int. Ed.* **2010**, *49*, 2371.
- [33] A. Hayashi, R. Ohtsubo, T. Ohtomo, F. Mizuno, M. Tatsumisago, *J. Power Sources* **2008**, *183*, 422.
- [34] K. P. Cai, M. K. Song, E. J. Cairns, Y. G. Zhang, *Nano Lett.* **2012**, *12*, 6474.
- [35] C. Nan, Z. Lin, H. Liao, M.-K. Song, Y. Li, E. J. Cairns, *J. Am. Chem. Soc.* **2014**, *136*, 4659.
- [36] X. Tao, J. Wang, Z. Ying, Q. Cai, G. Zheng, Y. Gan, H. Huang, Y. Xia, C. Liang, W. Zhang, Y. Cui, *Nano Lett.* **2014**, *14*, 5288.
- [37] Z. W. Seh, J. H. Yu, W. Li, P.-C. Hsu, H. Wang, Y. Sun, H. Yao, Q. Zhang, Y. Cui, *Nat. Commun.* **2014**, *5*, 5017.
- [38] X. Rui, H. Tan, Q. Yan, *Nanoscale* **2014**, *6*, 9889.
- [39] Y. Zhang, W. Sun, X. Rui, B. Li, H. T. Tan, G. Guo, S. Madhavi, Y. Zong, Q. Yan, *Small* **2015**, *11*, 3694.
- [40] S. Peng, L. Li, X. Han, W. Sun, M. Srinivasan, S. G. Mhaisalkar, F. Cheng, Q. Yan, J. Chen, S. Ramakrishna, *Angew. Chem. Int. Ed.* **2014**, *126*, 12802.
- [41] G. Zheng, Q. Zhang, J. J. Cha, Y. Yang, W. Li, Z. W. Seh, Y. Cui, *Nano Lett.* **2013**, *13*, 1265.
- [42] X. Tao, J. Wang, C. Liu, H. Wang, H. Yao, G. Zheng, Z. W. Seh, Q. Cai, W. Li, G. Zhou, C. Zu, Y. Cui, *Nat. Commun.* **2016**, *7*, 11203.
- [43] D. Lin, Z. Lu, P.-C. Hsu, H. R. Lee, N. Liu, J. Zhao, H. Wang, C. Liu, Y. Cui, *Energy Environ. Sci.* **2015**, *8*, 2371.
- [44] F. Wu, H. Kim, A. Magasinski, J. T. Lee, H.-T. Lin, G. Yushin, *Adv. Energy Mater.* **2014**, *4*, 1400196.
- [45] K. Zhang, L. Wang, Z. Hu, F. Cheng, J. Chen, *Sci. Rep.* **2014**, *4*, 6467.
- [46] G. M. Zhou, L. Li, D.-W. Wang, X.-Y. Shan, S. Pei, F. Li, H.-M. Cheng, *Adv. Mater.* **2015**, *27*, 641.
- [47] J.-S. Kim, T. H. Hwang, B. G. Kim, J. Min, J. W. Choi, *Adv. Funct. Mater.* **2014**, *24*, 5359.
- [48] Q. Zhang, Y. Wang, Z. W. Seh, Z. Fu, R. Zhang, Y. Cui, *Nano Lett.* **2015**, *15*, 3780.
- [49] B. Wang, S. M. Alhassan, S. T. Pantelides, *Phys. Rev. Appl.* **2014**, *2*, 034004.
- [50] Y. Li, K. Yan, H.-W. Lee, Z. Lu, N. Liu, Y. Cui, *Nat. Energy* **2016**, *1*, 15029.
- [51] W. Li, Q. Zhang, G. Zheng, Z. W. Seh, H. Yao, Y. Cui, *Nano Lett.* **2013**, *13*, 5534.